Characteristics of the Vertical Profiles of Dual-Frequency, Dual-Polarization Radar Data in Stratiform Rain

R. MENEGHINI

National Aeronautics and Space Administration/Goddard Space Flight Center, Greenbelt, Maryland

H. KUMAGAI

Communications Research Laboratory, Tokyo, Japan

(Manuscript received 15 April 1993, in final form 14 October 1993)

ABSTRACT

Airborne dual-wavelength and dual-polarization radar data are analyzed for measurements taken in stratiform rain in the western Pacific during September 1990. The focus of the paper is on the vertical profiles of the linear depolarization ratio, LDR (10 GHz); the reflectivity factor, dBZ (10 GHz); and the dual-frequency ratio, DFR (10, 34.45 GHz). Statistical characterizations of the maxima of these quantities and the relative locations at which they occur suggest that the eccentricity of the melting particles is fairly large and that the shape and size of the particles are correlated. To try to explain these features, two types of simulation are presented. In the first, a set of measured drop size distributions is used in the context of a standard model of the melting layer. Variations in snow density, as well as shape, size, and orientation distributions are used to study the relationship between these parameters and the radar measurements. To reduce the amount of ambiguity in the estimation, a second type of simulation is described in which the size distribution of the snow is estimated. Comparisons between the simulated and measured profiles indicate that radar measurements can be used to derive certain characteristics of the particle size and shape distributions in the melting layer.

1. Introduction

In this paper, airborne radar data are analyzed for the case of stratiform rain. The radar measurements consist of dual-frequency (10 and 34.45 GHz) and dual-polarized (10 GHz, co- and cross-polarized) returns measured simultaneously at near-nadir incidence over nearly identical scattering volumes. The objective is to account, in a semiquantitative way, for the dual-wavelength and polarimetric signatures in stratiform rain by using existing models of the melting layer coupled with a description of the hydrometeors that specifies their distributions of size, shape, and orientation.

We begin with an examination of the height profiles measured in stratiform rain of the radar reflectivity factor at X band, dBZ_X; the dual-frequency ratio, DFR; and the linear depolarization ratio, LDR_X. To summarize the data, statistics are given on the maximum values of these quantities and the locations at which they occur. The results show the following features: the maximum values of dBZ_X, DFR, and LDR_X that occur within the melting layer are moderately to well correlated with correlation coefficients between 0.6 and 0.9; the heights at which these maxima occur differ, however, with the maximum DFR occurring at ranges closest to the radar (farthest from the surface) and the maximum LDR at ranges farthest from the radar (closest to the surface) with the maximum dBZ_X located between these extremes.

To determine whether it is possible to duplicate the measured features of the data and extract information concerning the hydrometeors, measured raindrop size distributions are converted into snow and the particles are allowed to melt in accordance with model calculations. Simple parametric descriptions for the particle shape, size, and orientation are given. To reproduce the high correlations among the maximum values of LDR_X, DFR, and dBZ_X it is necessary to assume that the shape of the hydrometeor becomes more aspherical as the particle volume increases. The procedure, however, can be faulted in that the drop size distributions used in the simulation are unrelated to those that underlie the radar measurements. A second critique is that the solution is multivalued in the sense that a large number of particle and melting-layer models can be made qualitatively consistent with the measurements. To meet these difficulties we present an estimation procedure that is initialized by the reflectivity measurements in the snow. Measurements of the dual-frequency ratio in dry snow provide an indication of the particle size distribution without being highly sensitive

Corresponding author address: Robert Meneghini, NASA/Goddard Space Flight Center, Code 975, Greenbelt, MD 20771.

to particle shape. As such, the DFR provides an approximate separation between the shape and size parameters. This allows the particle size distribution to be fixed while studying the dependence of the profiles on the distributions of shape and orientation. The paper concludes with comparisons of estimated and measured profiles that show that while the comparisons are often qualitatively good, refinements in the models are needed for quantitative estimates.

2. Description of the instrument and experiment

The airborne radar data presented here were taken from measurements made over the western Pacific during September 1990. Aboard the National Aeronautics and Space Administration (NASA) DC-8 aircraft were a number of microwave radiometers, ranging in frequency from 10 to 90 GHz, and a dual-frequency radar that operates at 10 and 34.45 GHz. Descriptions of the hardware as well as preliminary analyses of the datasets can be found in Kumagai et al. (1993) and in Wang et al. (1994). The primary objective of the experiment was to support algorithm testing and development for the proposed spaceborne TRMM (Tropical Rainfall Measuring Mission) (Simpson et al. 1988).

Since this paper is concerned only with the radar data, the discussion is limited to this instrument alone. Built by the Communications Research Laboratory (CRL) of Japan in the late 1970s (Okamoto et al. 1982) after several experiments in Japan (Fujita et al. 1985), the radar was sent to the United States for a set of cooperative experiments between CRL and NASA (Meneghini et al. 1989; Kozu et al. 1991; Meneghini et al. 1992]. In 1989, the instrument was modified to measure the linear depolarization ratio (LDR) at the lower frequency (Kumagai et al. 1993); a subsequent modification provided LDR capability at both frequencies (Iguchi et al. 1992). For the measurements reported here only the single-frequency LDR data are available. The radar antennas for the two frequencies are nadir-mounted horn lens antennas with matched beamwidths of about 5°. Pulses of 0.5-μs duration, with nominal peak powers of 20 kW at 10 GHz and 10 kW at 34.45 GHz, are transmitted at a PRF (pulse repetition frequency) of 440 Hz. The echo power is oversampled at 0.2 μs over a range window of 22.2 km (740 range gates) at 10 GHz and 19.05 km (635 range gates) at 34.45 GHz. The outputs of the logarithmic detectors are averaged over 128 pulses; because the 10 GHz co- and cross-polarized returns are sampled over alternate pulses, the 128-pulse averages for the co- and cross-polarized channels are completed in 2(128)/440 s. During this period, two 128-pulse averages are performed for the 34.45-GHz returns.

3. Measurements in stratiform rain

a. Examples of profiles

Shown in Fig. 1 are 30 profiles of the 10-GHz and 34.45-GHz copolarized radar reflectivity factors dBZ_X (solid lines) and dBZ_{Ka} (dotted lines). Also shown in this figure are plots of the corresponding 10-GHz linear depolarization ratio LDR_X, represented by the dashed lines with a scale given by the right-hand ordinate. It should be noted that dBZ_X, LDR_X, and the dual-frequency ratio, DFR ($= dBZ_X - dBZ_{Ka}$), are obtained from the measured reflectivity factors where no compensation is made for attenuation. Each profile represents a 2-s average over the data so that the set of 30 represents a 1-min measurement period during which the aircraft flies about 12 km. The small deviations among the curves and the presence of a well-defined bright band, at a distance of about 8 km from the aircraft, indicate a region of vertically stratified rain. During this period the radar was pointed toward nadir and the sharply peaked return at about 12 km represents the copolarized surface return from the ocean. The surface spike provides a convenient way to distinguish the direct from the mirror-image return. Detectable components of the LDR_X are present in three distinct range intervals: within the melting layer as seen in both the direct (r = 7.5 km) and the mirror-image return (r = 16.7 km) and a component beginning just after the maximum of the copolarized surface return and extending out to 12.6 km. The focus of this paper is on components of the direct return only.

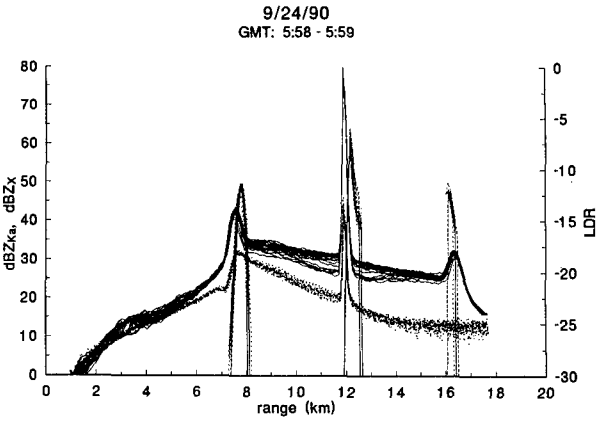

FIG. 1. The dBZ_X (solid lines), dBZ_{Ka} (dotted lines), and LDR_X (dashed lines, right-hand scale) for the time period 0558–0559 UTC 24 September 1990.

b. Statistics of dBZ_X, LDR_X, and DFR in the melting layer

To summarize the characteristics of the profiles of the type shown in Fig. 1, we compute the maximum values of dBZ_X, LDR_X, and DFR and the altitudes at which these maxima occur. The results from flight day 24 September 1990 are given in Figs. 2a and 2b showing scatterplots of $dBZ_{X\max}$ versus $LDR_{X\max}$ and $DFR_{\max}$ versus $LDR_{X\max}$, respectively. Each pair of points is taken from the maximum values of the profiles computed from a 2-s average. For this 3-h measurement

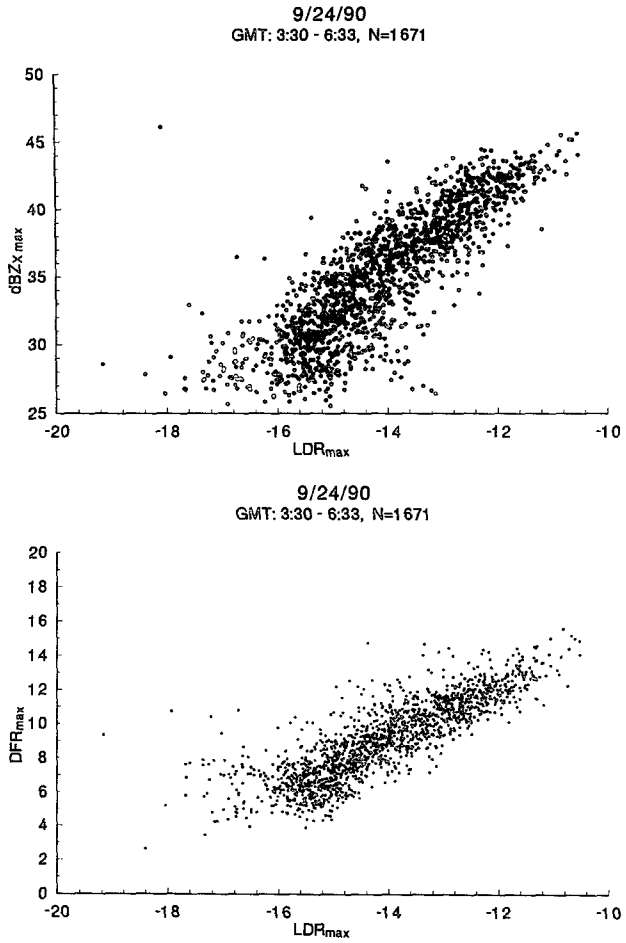

FIG. 2. (a) Scatterplot of the maxima of dBZ_X and LDR_X over stratiform rain for 1671 observations where an observation consists of a 2-s average. (b) Scatterplot of the maxima of DFR and LDR_X over the same observations as (a).

period, the algorithm selected about 55 min of data that met the following criteria: the incidence angle is within 5° of nadir; the maximum dBZ_X value exceeds 25 dBZ; and the profile exhibits a well-defined bright band. To illustrate the differences in heights at which the maxima of the LDR and DFR occur, a scatterplot of the heights of these maxima from the surface (km) is shown in Fig. 3 for stratiform rain measured on 17 September 1990. Statistics for three flight days are shown in Tables 1–3. Of particular importance for the simulation results presented later are the magnitude of the correlations between LDR_X and dBZ_X and between DFR and LDR_X as well as the mean values of these quantities. It should also be noted that the mean values of LDR_X agree well with previous measurements of this quantity at *S* band at low elevation angles (Illingworth and Caylor 1989; Frost et al. 1991).

Although quantitative results are presented in the next section, it is worthwhile first to identify possible reasons for the relatively high correlations among the quantities LDR_X, DFR, and dBZ_X. If the melting snow is randomly oriented, dBZ_X is relatively insensitive to particle shape but highly dependent on the particle volume and the fractional meltwater of the snow particle. In the absence of significant attenuation—an assumption that is usually valid for an airborne geometry at ranges near the top of the melting layer—the DFR is primarily determined by deviations from Rayleigh scattering effects at the high frequency. Like dBZ_X, the DFR is relatively insensitive to the drop shape so that both quantities should be well correlated and with magnitudes determined primarily by the phase state of the particles and the size distribution. In contrast, the LDR_X is relatively insensitive to particle size and is determined primarily by the shape, orientation, and the fractional melting of the particle (Hall et al. 1984; Bringi et al. 1986; Herzegh and Jameson 1992; Aydin and Giridhar 1991). If the dependence of these quantities on the phase state of the particle can be eliminated by considering only the maxima of LDR_X, DFR, and dBZ_X along the radar range direction, then the high correlations among these quantities can be achieved only if the size and shape of the particles are correlated. For the spheroidal particle model considered in this paper, this amounts to stating that either the mean eccentricity or the deviation from sphericity increases with the particle volume.

4. Analysis

a. Rayleigh theory

The linear depolarization ratio is defined as 10 $\log_{10}(Z_{xp}/Z_{cp})$, where the cross-polarized, Z_{xp}, and copolarized, Z_{cp}, reflectivity factors can be expressed as

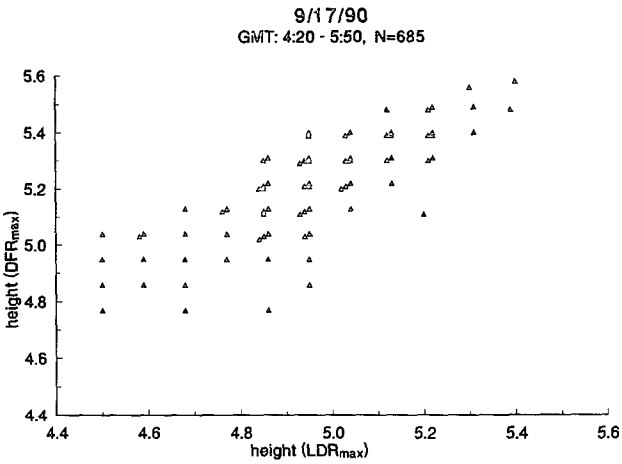

FIG. 3. Scatterplot of the heights at which the maxima of DFR and LDR_X occur for stratiform rain in the time period 0420–0550 UTC 17 September 1990.

TABLE 1. Means and standard deviations of the maximum values of dBZ_x, DFR, and LDR in stratiform rain.

Day	$\langle dBZ_X \rangle$	σ_{dBZ_X}	$\langle DFR \rangle$	σ_{DFR}	$\langle LDR \rangle$	σ_{LDR}	N
17 September 1990	33.8	4.1	7.3	2.5	−14.4	1.3	685
18 September 1990	36.8	3.5	9.1	2.7	−14.3	1.4	934
24 September 1990	35.1	4.6	9.1	2.3	−14.1	1.3	1671

$$Z_{xp(cp)}(h) = \iiint \langle \sigma_{xp(cp)} \rangle_\phi N(D; h) \times p_{\omega|D,h}(\omega|D; h) p_{\theta|h}(\theta|h) d\theta d\omega dD, \quad (1)$$

where $\langle \sigma_{xp} \rangle_\phi$ and $\langle \sigma_{cp} \rangle_\phi$ are the cross-polarized and copolarized backscattering cross sections averaged over the azimuthal angle ϕ, over which the particles are assumed to be uniformly distributed. Here, N is the distribution for the equivolume melted drop diameter D and $p_{\omega|D,h}(\omega|D; h)$, $p_{\theta|h}(\theta|h)$ are the probability density functions for the shape parameter ω (conditioned on D) and for the canting angle θ, respectively. In this paper the canting angle is defined as the angle between the symmetry axis of the particle and the vertical. The distributions have been written as a function of the height h to allow for variations in altitude. It is clear from an examination of Figs. 2a and 2b that the function $p_{\omega|D}(\omega|D; h)$ is crucial in determining the correlations between the radar measurements as this distribution links the particle shape and size. The distribution must be sufficiently general to include important special cases—for example, that it reduce to a deterministic relationship between size and shape for raindrops or that it allow for the independence of size and shape. If we limit the particle shape to that of a prolate or oblate spheroid where $2a/2b$ is the ratio of the length of the particle along the symmetry axis to that along an orthogonal axis, then the distribution must also be such that there is zero probability that either $a = 0$ or $b = 0$. One way to satisfy these criteria is to let a/b be lognormally distributed with $\omega = \ln(a/b)$, so that ω is normally distributed:

$$p_{\omega|D,h}(\omega|D; h) = \frac{1}{\sigma(D)(2\pi)^{1/2}} \times \exp\left(- \frac{\{\omega - \beta(h) \ln[f(D, h)]\}^2}{2\sigma^2(D)} \right). \quad (2)$$

An important special case of (2) is obtained by assuming that the mean, $\beta(h) \ln[f(D, h)]$, and variance σ^2 of ω are independent of D, so that $p_{\omega|D,h}(\omega|D; h) = p_{\omega|h}(\omega|h)$. Substituting this into the definitions for Z_{xp} and Z_{cp}, using the Rayleigh approximations for $\langle \sigma_{xp} \rangle_\phi$ and $\langle \sigma_{cp} \rangle_\phi$ (Ishimaru 1978) and noting that the dependence on D for both quantities is contained in the term $D^6 N(D)$ it follows that LDR is independent of the drop size distribution. Further assuming that $\sigma \to 0$, $\beta = 1$, then $p_{\omega|h}(\omega|h) \to \delta\{\omega - \ln[f(h)]\}$, where δ is the delta function that is equivalent to stating that the particles all have an identical shape specified by $a/b = f(h)$. If it is further assumed that the canting angle is uniformly distributed, the LDR reduces to a function of eccentricity and the refractive index only. Plots of LDR for this case are shown in Fig. 4 versus the ratio a/b, where values $a/b < 1$ correspond to oblates and $a/b > 1$ prolates, and are similar to those presented by Atlas et al. (1953). The 11 curves represent different melting fractions (by volume) where the lowermost curve represents the case of dry snow (density) of 0.2 g cm^{-3} and the topmost curve the case of water. For the intermediate curves, the fractional meltwater by volume changes by 10% from curve to curve. In computing the refractive index of the mixture, the Maxwell Garnett (MG) (Maxwell Garnett 1904; Bohren and Battan 1982) formula is used where the snow is taken as the matrix with water inclusions. Although the curves of Fig. 4 can be used to explain several characteristics of the measurements, what cannot be explained under this assumption are the relatively high correlations between $dBZ_{X\max}$ and $LDR_{X\max}$ that are observed in the measurements (Fig. 3a). To do this, it is necessary to assume that the shape and size of the particles are correlated.

In the simulations given in sections 4c and 5b, two models for the particle shape distribution are used. For the first model, the mean shape of dry snow aggregates is taken to be spherical but with a variance about the mean shape that increases with particle size. This case can be obtained from (2) by setting $\mu \equiv \beta \ln[f(D)]$

TABLE 2. Correlation coefficients among the maximum values of dBZ_X, DFR, and LDR in the melting layer.

Day	ρ (dBZ_X, LDR)	ρ (dBZ_X, DFR)	ρ (LDR, DFR)
17 Sep 1990	0.51	0.65	0.60
18 Sep 1990	0.83	0.84	0.88
24 Sep 1990	0.85	0.84	0.83

TABLE 3. Location of the maxima Lm of dBZ_X, DFR, and LDR as measured from the surface (km).

Day	Lm (dBZ_X)	Lm (DFR)	Lm (LDR)
17 September 1990	5.05	5.14	4.9
18 September 1990	4.78	4.88	4.64
24 September 1990	4.36	4.46	4.2

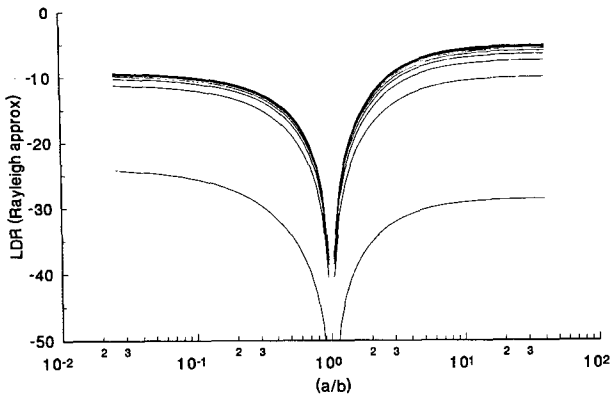

FIG. 4. LDR versus (b/a) for snow–water combinations using the Maxwell Garnett mixing formula: lowermost curve is dry snow and uppermost is water with a 10% increase in water by volume from curve to curve (Rayleigh approximation).

$= -\sigma^2/2$ and by taking σ to be proportional to D^ν, $\nu > 0$; since $\langle a/b \rangle = \exp(\mu + \sigma^2/2)$, then $\langle a/b \rangle = 1$. A second model assumes that a 1:1 correspondence exists between shape and size. This case can be obtained from (2) by setting β to 1 and letting σ tend to 0 so that $p_{\omega|D,h}(\omega|D, h) \to \delta\{\omega - \ln[f(D, h)]\}$. It will be shown later that either distribution can account, in a qualitative manner, for the experimentally observed correlations.

b. *Particle and melting-layer models*

In simulating the radar profiles, measured raindrop size distributions (courtesy of Dr. Jurg Joss) are converted into snow and allowed to fall and melt in accordance with the model described by Ekpenyong and Srivastava (1970) and Yokoyama and Tanaka (1984). For these calculations, aggregation and drop breakup are not included. Because the largest raindrop size is 5.3 mm and because of the 1:1 relationship between the snow particles and raindrops, the maximum equivolume snow diameter is given by $5.3(\rho_w/\rho_s)^{1/3}$ mm, where ρ_w, ρ_s are the mass densities of water and snow. To approximate measurements of the temperature profile, a lapse rate of 2°C km^{-1} is used over the top 300 m of the melting layer and a lapse rate of 6°C km^{-1} below this (Willis and Heymsfield 1989). The primary variable in the model is the density of snow that along with the measured raindrop distribution determines the size and velocity distributions of the snow particles and the rate of melting. Although the results given in this paper were obtained by assuming that the snow density is a constant independent of the size, cases have been computed where the snow density is given as a function of size (Passarelli and Srivastava 1979; Klaasen 1988). For the polarimetric radar signature, the quantities of greatest importance are the distributions of shape and orientation. In the snow, the particles are taken to be randomly oriented, while far below the melting level the raindrops are assumed to be highly oriented along the vertical (Beard and Jameson 1983; Frost et al. 1991). Between these extremes a linear interpolation formula for the orientation distribution is used. For the distribution of shapes, the models discussed in section 4a are used. The order of calculations proceeds as follows: for a particular height and equivolume diameter D, the melting model, the snow density, and the mixing formula determine the refractive index of the particle. In the usual case, moreover, D determines the eccentricity of the oblate or prolate particle so that the azimuthally averaged cross sections can be computed as a function of the canting angle θ. As the cross sections are known as a function of size, canting angle, and fractional meltwater, they can be used to calculate the profiles of LDR and dBZ for arbitrary distributions of particle size and canting angle. It should be noted, however, that the calculations for the cross sections must be repeated if the size–shape relation is changed.

c. *Simulation of the statistics*

Before presenting models for which the shape and size are correlated, it should be noted that several examples were computed for which the size and shape were assumed to be independent. In the first case the distribution for the shape parameter ω [Eq. (2)] is determined by setting $\mu \equiv \beta \ln f = -\sigma^2/2$ with $\sigma = 0.7$, so that the mean particle shape is spherical with a deviation that is independent of drop size. A second example was computed by assuming the particles to be identically shaped, is a/b is constant, which can be obtained from (2) by assuming that $\sigma \to 0$ and f is constant. In both cases, the scatterplots of dB$Z_{X\max}$ versus LDR$_{\max}$ show a small but negative correlation.

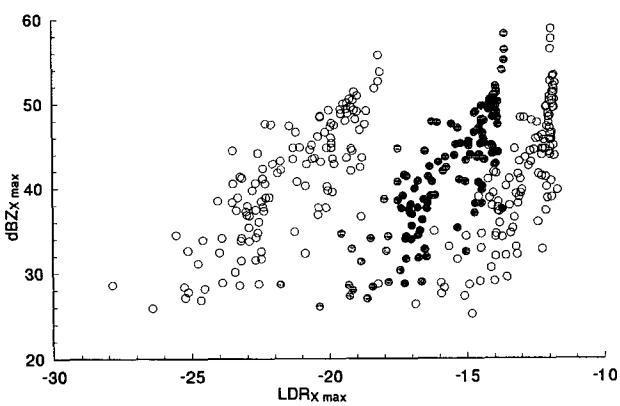

FIG. 5. Scatterplots of the maxima of dBZ and LDR for simulations where the standard deviation from sphericity is proportional to the equivolume diameter. Rightmost open dots correspond to $\alpha = 0.3$, solid dots $\alpha = 0.2$, and leftmost open dots $\alpha = 0.1$ (Rayleigh approximation).

For the scatterplots shown in Fig. 5, $\mu \equiv \beta \ln[f(D)] = -\sigma^2/2$ with $\sigma = \alpha D$, which is equivalent to assuming that the mean particle shape is spherical, $\langle a/b \rangle = 1$, but with a deviation from sphericity that increases with particle diameter. For the three sets of scattergrams shown, the values of α are taken to be 0.1, 0.2, and 0.3, where the largest value of α corresponds to the set of points with the largest mean value of LDR and conversely. Although the scattergram for $\alpha = 0.3$ is qualitatively similar to the measurements, the calculations depend on the Rayleigh approximation, which is inaccurate for large, wet snow particles and inapplicable to calculations of the DFR. For the results presented in the remainder of the paper the T-matrix method is used (Barber and Hill 1990).

As noted in section 4a, a second way to model the correlation between drop shape and size is to assume a 1:1 relation between the eccentricity and the equivolume drop diameter. A simple function of this type is a modification of the Pruppacher and Beard (1970) formula for raindrops:

$$f(D_{eqs}) = 1.03 - 0.062 p D_{eqs}, \qquad (3)$$

where f is equal to b/a for a prolate spheroid, and a/b for an oblate spheroid and where $2a$ is the length of the particle along the axis of symmetry. Equation (3) reduces to the Pruppacher–Beard relationship for $p = 1$ and $f = a/b$. The quantity D_{eqs} is the equivolume diameter (mm) of the actual particle and not that of the melted particle so that as the particle melts, it becomes more spherical (f increases). A limitation on (3) arises from lack of convergence of the T-matrix method for large, aspherical particles. To avoid this, f is set equal to 0.3 whenever (3) yields a value smaller than this. Shown in Figs. 6a and 6b are scatterplots of the quantities $dBZ_{X\max}$, $LDR_{X\max}$, and $DFR_{\max}$ using the T-matrix method and the shape–size relationship given by (3); in each plot two sets of curves are shown corresponding to the value of p equal to 1 and 2. In both cases, the correlations and locations of the maxima are similar to the measured values given in Tables 1–3. However, the larger value of eccentricity is needed ($p = 2$) in order to yield values of LDR close to those of the measurements.

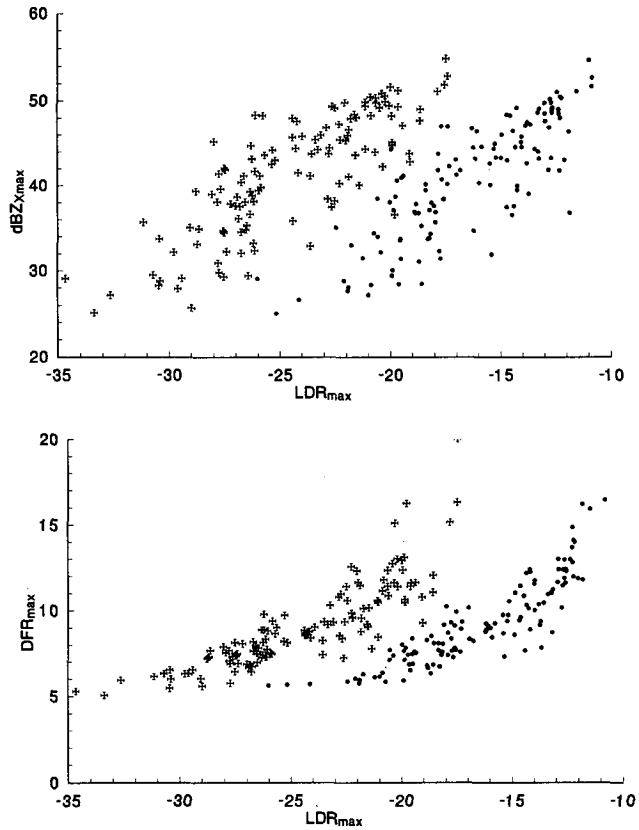

FIG. 6. (a) Scatterplots of the maxima of dBZ_X and LDR_X for a simulation where the shape is a function of size [Eq. (3)]. Crosses correspond to $p = 1$ and dots to $p = 2$. (b) Same as (a) but for the maxima of DFR and LDR_X.

5. A profiling estimation procedure

a. Description

The modeling described in the last section can be criticized in that the size distributions used in the simulation bear no relationship to the distributions that underlie the radar measurements. In the procedure described here, the retrieval is initialized by matching the simulation to the measurements in dry snow; an offshoot of the approach is that it allows a partial separation between the parameters of shape and size. This capability of separating the two parameters is based on the fact that the copolarized returns from the dry snow layer are relatively independent of shape if the orientations of the particles are random. Under this assumption, the dual-wavelength data provide an estimate of the snow size distribution.

Computations using the T-matrix method have shown that the DFR ($= dBZ_X - dBZ_{Ka}$) for dry spheroidal snow particles exhibits only small variations as a function of the axial ratio a/b if the mass of the particle is held constant. For example, at 10 GHz, for equivolume melted drop diameters up to 5 mm, the copolarized cross section varies by less than 2.3 dB as the a/b is varied from 1 to 5. These results also hold for 34.45 GHz if the melted drop diameter is 3 mm or less. This behavior implies that the DFR is primarily a function of the snow size distribution, SSD, and that a spherical model for the particles is sufficient to estimate the SSD. The first step in the estimation procedure is to derive the size distribution of the snow from the measured values of dBZ_X and DFR. As the attenuation in dry snow is small, the measured and actual reflectivity factors are approximately the same. However, if a substantial amount of cloud liquid water (CLW) is present above the melting layer, caution is needed. For

example, a CLW of 0.25 g m^{-3} over a 2-km layer at T = 0°C will increase the DFR by about 1 dB. In the examples that will be presented, the DFR just above the melting layer is 5 dB or greater so that, as a first approximation, the contribution from the cloud liquid water can be neglected. Using a gamma distribution (Ulbrich 1984) of snow then

$$N_s(D) = N_0 D^{\mu} \exp\left[-(3.67 + \mu)\frac{D}{D_0}\right], \quad (4)$$

where D is the equivolume melted diameter of the snow particle, and D_0 is the median mass diameter (melted) of the distribution. Expressing the DFR as a function of the cross sections and the drop size distribution (DSD) shows that it is independent of N_0. Therefore, if a snow density ρ_s and a DSD shape parameter μ are assumed, the DFR can be used to estimate D_0. The coefficient N_0 is obtained from D_0 and the definition of Z_X. This type of approach has been used by a number of authors in applications to both rain and snow (Atlas and Ulbrich 1974; Goldhirsh and Katz 1974; Gossard and Strauch 1983; Gosset and Savageot 1992). The estimation procedure can be summarized by the following equations:

$$\hat{f}(D_0, \rho_s, \mu) = \frac{Z_K}{Z_X}, \quad (5)$$

$$f(D_0, \rho_s, \mu) = \frac{\int \sigma_{cp}(\lambda_K, \rho_s, D) D^{\mu} \exp[-(3.67 + \mu)(D/D_0)]dD}{\int \sigma_{cp}(\lambda_X, \rho_s, D) D^{\mu} \exp[-(3.67 + \mu)(D/D_0)]dD}, \quad (6)$$

$$N_0(D_0, \rho_s, \mu) = \frac{\pi^5 |K_w|^2 Z_X}{[\lambda_X^4 \int \sigma_{cp}(\lambda_X, \rho_s, D) D^{\mu} \times \exp[-(3.67 + \mu)(D/D_0)]dD]}. \quad (7)$$

From (6) lookup tables of f versus D_0 are generated for fixed values of μ and ρ_s. Equating the theoretical, f, to the measured value, $\hat{f}$ [Eqs. (5) and (6)], D_0 is obtained as a function of μ and ρ_s. To illustrate this graphically, plots of Z_K/Z_X ($=10^{-\mathrm{DFR}/10}$) versus D_0 are computed from (6) for different snow densities and with $\mu = 2$ (Fig. 7a). In contrast to the case of raindrops, the curves are monotonic in D_0 for all but small values of D_0, so that given ρ_s, μ, and a measurement of DFR, a unique solution for D_0 usually exists (Meneghini et al. 1992). In Fig. 7b curves of Z_K/Z_X versus D_0 are plotted for a fixed snow density of 0.2 g cm^{-3} for the cases of μ = 0 and 8. The data points on the figure were computed by converting 180 measured DSDs into size distributions of snow (SSD) with ρ_s = 0.2 g cm^{-3} using the assumption that no drop breakup or aggregation occurs.

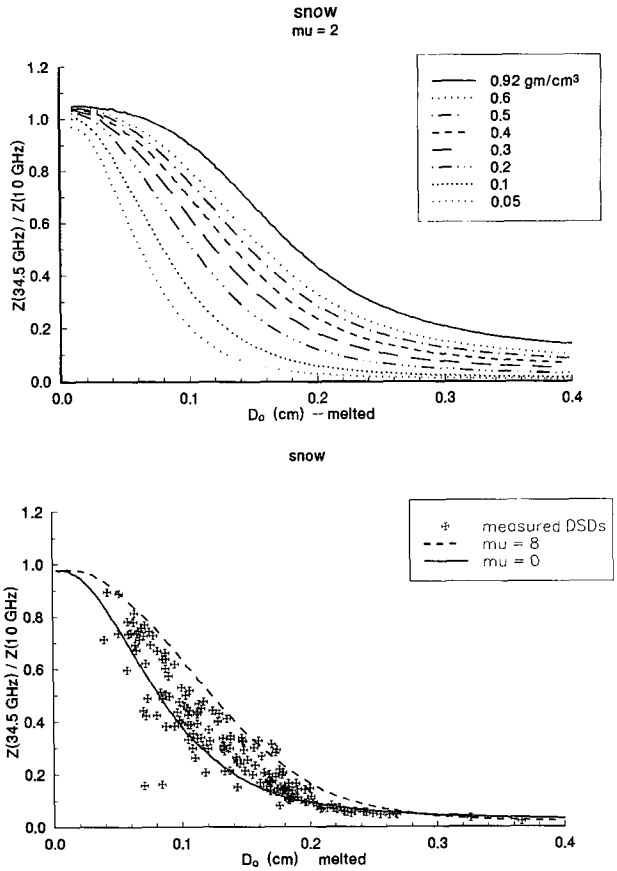

FIG. 7. (a) The $Z(34.5\ \mathrm{GHz})/Z(10\ \mathrm{GHz})$ versus melted median mass diameter (cm) for eight values of snow density for $\mu = 2$. (b) The $Z(34.5\ \mathrm{GHz})/Z(10\ \mathrm{GHz})$ versus melted median mass diameter (cm) for μ = 0, 8 and ρ_s = 0.2 g cm^{-3}.

If the number of possible values of μ and ρ_s are J and K, respectively (which are assumed to be range independent), and if the range gates from the storm top to the leading edge of the melting layer run from 1 to I ($i = 1, \cdots, I$), then the JK DSD profiles that are consistent with the measured radar data can be written

$$\{N_0(\mu_j, \rho_k; r_i), D_0(\mu_j, \rho_k; r_i), i = 1, \cdots, I\}; \quad j = 1, \cdots, J; \quad k = 1, \cdots, K. \quad (8)$$

It should be noted that if ρ_s is specified as a function of the size of the snow (Passarelli and Srivastava 1979), then $K = 1$ and a number of DSD profiles reduces to J. To extend the estimation into the melting layer, the DSD found at the top of the layer ($i = I$) is used to estimate the radar profiles below by assuming that no coalescence, growth, or drop breakup occurs.

b. *Comparisons of measured and simulated profiles*

An example of a measured set of profiles is shown in Fig. 8 where $\mathrm{dB}Z_X$, DFR, and LDR (right-hand

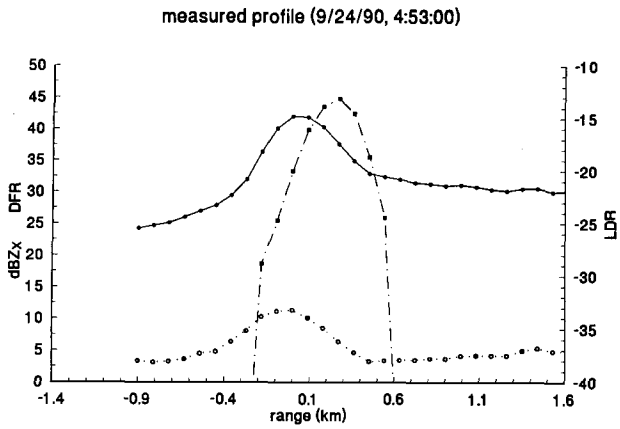

FIG. 8. Measured profiles of dBZ_X (solid line), DFR (dotted line), and LDR (dash–dot, right-hand scale) from 0453:00 UTC 24 September 1990.

ordinate) are plotted over a 3-km range with the maximum DFR value selected as the origin of the abscissa. For these profiles the maxima of dBZ_X and DFR, equal to 42 and 12 dB, respectively, occur at the same range gate, whereas the LDR maximum, of −13 dB, occurs three gates (270 m) below. The height at which the snow begins to melt is taken to be the gate at which a measurable value of LDR is first detected. For the present case, this occurs three gates above the maximum DFR and dBZ_X values. The values of dBZ_X and DFR in the gate just above this are used to estimate the snow size distribution for different snow densities and values of μ. The three sets of simulated profiles shown in Figs. 9a–c correspond to snow densities of 0.05, 0.1, and 0.2 g cm^{-3}, respectively. In all cases the particles are assumed to be prolate spheroids with a shape factor p [Eq. (3)] equal to 2. The Maxwell Garnett formula is used to compute the refractive index of the mixed-phase particles. As noted earlier, a piecewise constant lapse rate is used to approximate measured temperature profiles. In plots of the simulated profiles, the top of the melting layer is arbitrarily taken to be 5 km above the surface.

In the snow, the simulated profiles agree well with the measurements because, in effect, a circular procedure is used: the measured values of dBZ_X and DFR yield estimates of the snow size distributions that, in turn, are used to generate the profiles of dBZ_X, DFR, and LDR_X. What should be noted is that the reconstruction of the profiles is accomplished equally well

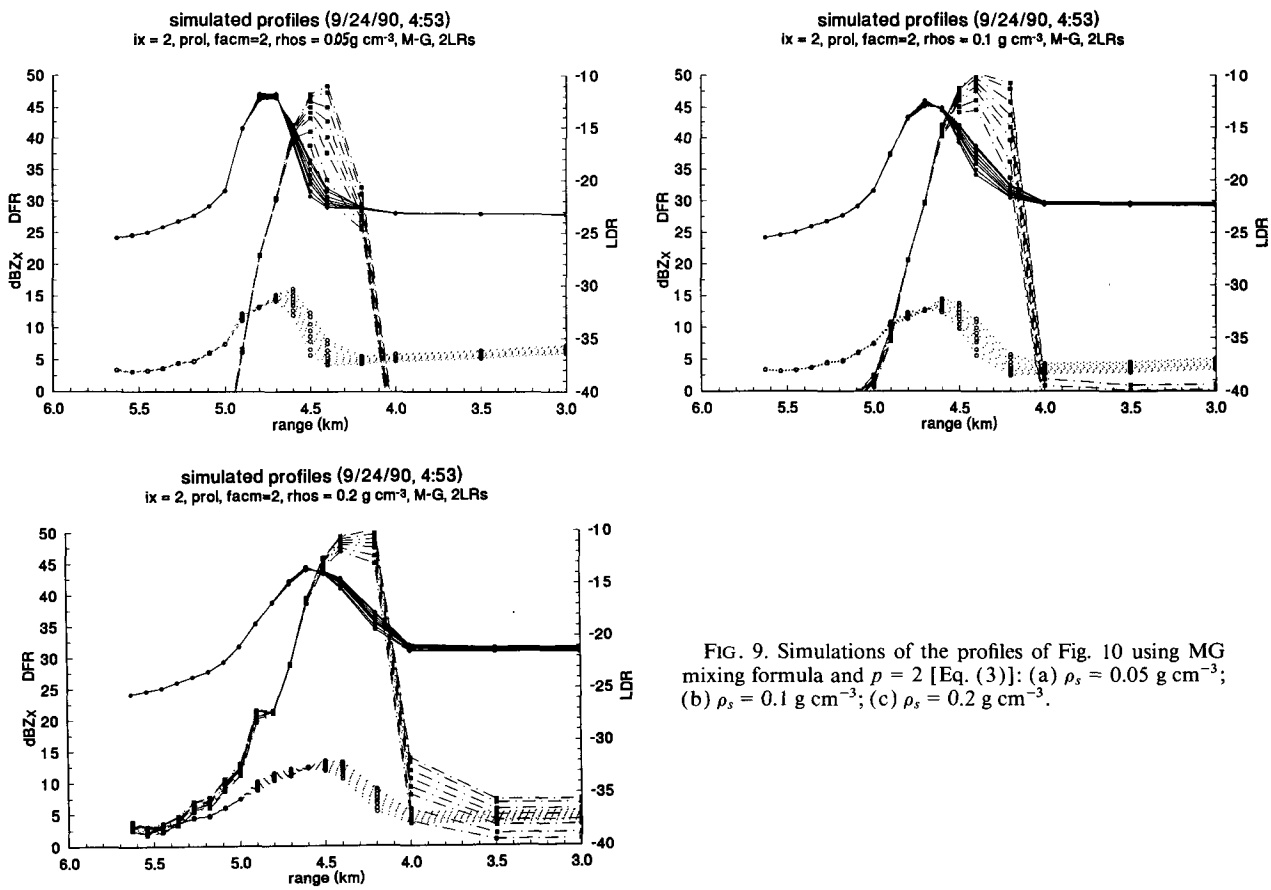

FIG. 9. Simulations of the profiles of Fig. 10 using MG mixing formula and $p = 2$ [Eq. (3)]: (a) $\rho_s = 0.05$ g cm^{-3}; (b) $\rho_s = 0.1$ g cm^{-3}; (c) $\rho_s = 0.2$ g cm^{-3}.

for any snow density (and any value of μ) by an appropriate change in the snow size distribution parameters N_0 and D_0. In each panel of Fig. 9 the eight profiles of dBZ_X, DFR, and LDR_X correspond to values of μ given by $(-0.5, 0, 1, 2, 3, 4, 6, 8)$. Since large values of μ imply a scarcity of large drops, the dBZ_X, LDR_X, and DFR all decrease as μ increases; this effect, however, is noticeable only over the lower portion of the melting layer.

Comparisons between the simulated and measured profiles show that the results of all three simulations are reasonable in the sense that the shapes and relative locations of the curves are similar. Closer inspection shows the profiles of dBZ_X and DFR for the $\rho_s = 0.05$ g cm^{-3} case (Fig. 9a) to be more highly peaked and narrow than the measurements, while just the opposite is true of the $\rho_s = 0.2$ g cm^{-3} case of Fig. 9c. Judged according to the shapes of the measured profiles, the case of $\rho_s = 0.1$ g cm^{-3}, Fig. 9b, appears to be the best. Despite this, a comparison with Fig. 8 indicates that the peak value of dBZ in Fig. 9b is approximately 3 dB larger than the measured value. The peak values of dBZ_X and LDR in Fig. 9b are, like the measurements, separated by about 300 m; to some extent, however, the location and shape of the trailing edge of the simulated LDR profile can be controlled by the choice of the orientation distribution of the drops.

A second set of measured profiles is shown in Fig. 10 by the heavy solid lines. Comparisons of the two examples reveal several differences. The maxima of the dBZ_X, DFR, and LDR_X are, respectively, 33, 7.5, and -14.7 dB, as compared to the maxima of Fig. 8 (42, 12, and -13 dB). The relatively small value of DFR of 5 dB just above the melting layer and the narrow width of the profiles suggest a median mass diameter smaller than that found in the previous example. Superimposed on the measurements in Fig. 10 are the simulations results (lowermost dashed lines) using a snow density of 0.2 g cm^{-3}, $p = 2$ and $\mu = 2$; with the exception of the different snow size distributions, the parameters used to generate the simulations of Fig. 10 and Fig. 9c are identical. Comparisons of measured and simulated profiles show that the simulation is able to reproduce the measurements fairly well over the growing portion of the dBZ_X curve and out to about the third range gate beyond the peak value. Thereafter the measured dBZ_X profile quickly stabilizes to a value of about 27 dB while the simulated profile decreases to a value of 22 dB. Possible mechanisms that may explain the discrepancies are aggregation or a change in shape from prolate to oblate drops. Of course, the replacement of the prolate spheroids with oblates at the lower edge of the melting layer is not only reasonable but correct; this change, however, only increases dBZ_X by about 1 dB. A second possibility is aggregation of hydrometeors in the lower portion of the melting layer: examples of this are shown by the two uppermost sets of dashed lines in Fig. 10 where aggregation is

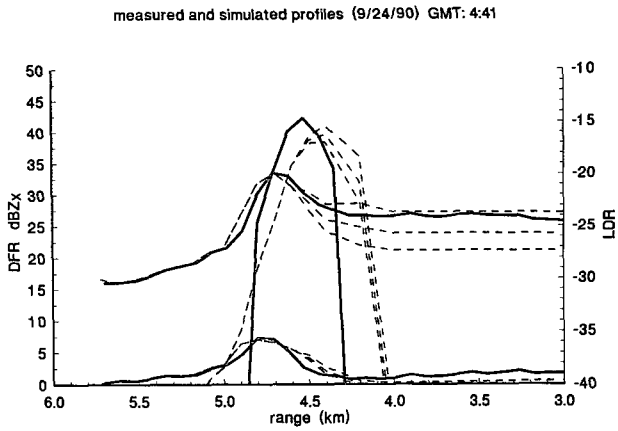

FIG. 10. Measured (solid lines) and simulated (dashed lines) profiles versus range for a measurement made at 0441 UTC 24 September 1990.

modeled simply by increasing the median mass diameter of the particles in the three gates just below the maximum of dBZ_X. While these curves indicate that the introduction of aggregation improves the agreement between the measured and simulated curves, it also illustrates the additional ambiguities in the estimation procedure when aggregation (or drop breakup) is considered.

6. Summary and discussion

The insensitivity of the DFR and dBZ_X to shape effects in dry, randomly oriented snow allows an estimate of the size distribution for snow aggregates or graupel that can be expressed as a function of the snow density and the DSD parameter μ. Using the inferred DSD and a simple melting model, the distributions of particle shape and orientation can be varied to test whether qualitative agreement can be obtained within the melting layer between the measured and simulated profiles of DFR, dBZ_X, and LDR_X. A constraint on the type of shape distribution was inferred from the experimental data that suggest that size and eccentricity are positively correlated. Comparisons between the measured and simulated profiles show that some features of the experimental data can be reproduced; in particular, the maximum LDR_X and the relative locations of the LDR_X, DFR, and dBZ_X maxima of the simulated curves often compare well with the measurements. As shown in section 4c, some of the statistical characteristics of the measurements also can be recovered. The parameters in the model described in section 5b that yielded the best agreement are prolate spheroids of high eccentricity that are made to correspond in a 1:1 relationship with particle size. To reproduce the shapes of the DFR and dBZ profiles, the Maxwell Garnett mixing formula and snow densities in the range from 0.05 to 0.2 g cm^{-3} were used. The

question remains, however, as to whether the procedures described in sections 4 and 5 can be used to infer shape, size, and orientation distributions of the hydrometeors as well as the snow density. To try to answer this question, it is necessary to distinguish the various components of the model. The estimation of the snow size distribution seems to be on secure ground as long as the hydrometeors are randomly oriented. Although single crystals do exhibit a preferred orientation, aggregates and graupel are more randomly oriented because of tumbling and rocking motions (Illingworth and Caylor 1989; Frost et al. 1991). For most of the profiles examined here the DFR just above the melting layer is greater than 5 dB, which, according to Fig. 7a, implies median mass snow diameters greater than 2 mm and is consistent with aggregates being the primary scatterers. Although the assumption that the shape and size of the particles are correlated is consistent with the experimental results, the explicit form assumed in (3) between these two parameters is somewhat arbitrary and a 1:1 relationship between size and shape is not needed to reproduce positive correlations between dBZ_X and LDR_X. In particular, it was shown in section 4c that a shape distribution that is spherical in the mean, but with a deviation from sphericity that increases with particle size, is sufficient to give positive correlations. A related problem is that the shapes of aggregates or graupel are not well approximated by spheroids so that we can speak only of an effective eccentricity of the particle. One other source of ambiguity is the choice of a mixing formula and the order in which the constituents are introduced into it. Aggregation and drop breakup further complicate the retrieval. From these considerations it must be concluded that while the radar profiles provide information as to the snow size distribution and constraints on the relationship between shape and size, the procedure described here is not sufficient to infer a detailed description of the particles in the melting layer.

Acknowledgments. We wish to thank the members of the airborne experimental team and the Medium Altitude Branch of NASA Ames Research Center.

REFERENCES

Atlas, D., and C. W. Ulbrich, 1974: The physical basis for attenuation rainfall relationships and the measurement of rainfall parameters by combined attenuation and radar methods. *J. Rech. Atmos.*, **8,** 275–298.

——, M. Kerker, and W. Hitschfeld, 1953: Scattering and attenuation by non-spherical atmospheric particles. *J. Atmos. Terr. Phys.*, **3,** 108–119.

Aydin, K., and V. Giridhar, 1991: Polarimetric C-band radar observables in melting hail: A computational study. Preprints, *25th Conf. on Radar Meteorology,* Paris, France, Amer. Meteor. Soc., 733–736.

Barber, P. W., and S. C. Hill, 1990: *Light Scattering by Particles: Computational Methods.* World Scientific Publishing Co., 261 pp.

Beard, K. V., and A. R. Jameson, 1983: Raindrop canting. *J. Atmos. Sci.*, **40,** 448–454.

Bohren, C. F., and L. J. Battan, 1982: Radar backscattering of microwaves from spongy ice spheres. *J. Atmos. Sci.*, **39,** 2623–2628.

Bringi, V. N., J. Vivekanandan, and J. D. Tuttle, 1986: Multiparameter radar measurements in Colorado convective storms. Part II: Hail detection. *J. Atmos. Sci.*, **43,** 2564–2577.

Ekpenyong, B. E., and R. C. Srivastava, 1970: Radar characteristics of the melting layer: A theoretical study. Tech. Report No. 16, Laboratory for Atmos. Probing, University of Chicago, 40 pp. [Available from Department of the Geophysical Sciences, University of Chicago, Chicago, IL 60637.]

Frost, I. R., J. W. F. Goddard, and A. J. Illingworth, 1991: Hydrometeor identification using cross polar radar measurements and aircraft verification. Preprints, *25th Conf. on Radar Meteorology,* Paris, France, Amer. Meteor. Soc., 658–661.

Fujita, M., K. Okamoto, S. Yoshikado, and K. Nakamura, 1985: Inference of rain rate profile and path-integrated rain rate by an airborne microwave rain scatterometer. *Radio Sci.*, **20,** 631–642.

Goldhirsh, J., and I. Katz, 1974: Estimation of raindrop size distribution using multiple wavelength radar systems. *Radio Sci.*, **9,** 439–446.

Gossard, E. E., and R. G. Strauch, 1983: *Radar Observation of Clear Air and Clouds.* Elsevier, 280 pp.

Gosset, M., and H. Savageot, 1992: A dual-wavelength radar method for ice–water characterization in mixed-phase clouds. *J. Atmos. Oceanic Technol.*, **9,** 538–547.

Hall, M. P. M., J. W. F. Goddard, and S. M. Cherry, 1984: Identification of hydrometeors and other targets by dual-polarization radar. *Radio Sci.*, **19,** 132–140.

Herzegh, P. H., and A. R. Jameson, 1992: Observing precipitation through dual-polarization measurements. *Bull. Amer. Meteor. Soc.*, **73,** 1365–1374.

Iguchi, T., R. Meneghini, and H. Kumagai, 1992: Radar depolarization signatures of rain in cumulus clouds measured with a dual-frequency radar. *IGARSS '92,* IEEE/U.R.S.I., 1728–1730.

Illingworth, A. J., and I. J. Caylor, 1989: Cross polar observations of the bright band. *Proc. 24th Conf. on Radar Meteorology,* Tallahassee, Amer. Meteor. Soc., 323–327.

Ishimaru, A., 1978: *Wave Propagation and Scattering in Random Media.* Vol. 1. Academic Press, 250 pp.

Klaasen, W., 1988: Radar observations and simulation of the melting layer of precipitation. *J. Atmos. Sci.*, **45,** 3741–3753.

Kozu, T., K. Nakamura, R. Meneghini, and W. C. Boncyk, 1991: Dual-parameter radar rainfall measurement from space: A test result from an aircraft experiment. *IEEE Trans. Geosci. Remote Sens.*, **29,** 690–703.

Kumagai, H., R. Meneghini, and T. Kozu, 1993: Preliminary results from multiparameter airborne rain radar measurement in the western Pacific. *J. Appl. Meteor.*, **32,** 431–440.

Maxwell Garnett, J. C., 1904: Colors in metal glasses and in metallic films. *Philos. Trans. Roy. Soc.*, **A203,** 385–420.

Meneghini, R., K. Nakamura, C. W. Ulbrich, and D. Atlas, 1989: Experimental tests of methods for the measurement of rainfall rate using an airborne dual-wavelength radar. *J. Atmos. Oceanic Technol.*, **6,** 637–651.

——, T. Kozu, H. Kumagai, and W. C. Boncyk, 1992: A study of rain estimation methods form space using dual-wavelength radar measurements at near-nadir incidence over ocean. *J. Atmos. Oceanic Technol.*, **9,** 364–382.

Okamoto, K., S. Yoshikado, H. Masuko, T. Ojima, N. Fugono, K. Nakamura, J. Awaka, and H. Inomata, 1982: Airborne microwave rain scatterometer/radiometer. *Int. J. Remote Sens.*, **3,** 277–294.

Passarelli, R. E., and R. C. Srivastava, 1979: A new aspect of snowflake aggregation. *J. Atmos. Sci.*, **36,** 484–493.

Pruppacher, H. R., and K. V. Beard, 1970: A wind tunnel investigation of the internal circulation and shape of water drops falling at terminal velocity in air. *Quart. J. Roy. Meteor. Soc.*, **96,** 247–256.

Simpson, J., R. F. Adler, and G. North, 1988: A proposed Tropical Rainfall Measuring Mission (TRMM) satellite. *Bull. Amer. Meteor. Soc.,* **69,** 278–295.

Ulbrich, C. W., 1984: Natural variations in the analytic form of the raindrop size distribution. *J. Climate Appl. Meteor.,* **22,** 1764–1775.

Wang, J. R., R. Meneghini, H. Kumagai, T. T. Wilheit, W. C. Boncyk, P. Racette, J. Tesmer, and B. Maves, 1994: Airborne active and passive microwave observations of Supertyphoon Flo. *IEEE Trans. Geosci. Remote Sens.,* submitted.

Willis, P. T., and A. J. Heymsfield, 1989: Structure of the melting layer in mesoscale convective system stratiform precipitation. *J. Atmos. Sci.,* **46,** 2008–2025.

Yokoyama, T., and H. Tanaka, 1984: Microphysical processes of melting snowflakes detected by two-wavelength radar. *J. Meteor. Soc. Japan,* **62,** 650–666.